CHEMISTRY OF MATERIALS

pubs.acs.org/cm

Article

Nature of the Superionic Phase Transition of Lithium Nitride from Machine Learning Force Fields

Gabriel Krenzer, Johan Klarbring, Kasper Tolborg, Hugo Rossignol, Andrew R. McCluskey, Benjamin J. Morgan,* and Aron Walsh*

Cite This: *Chem. Mater.* 2023, 35, 6133−6140

Read Online

ACCESS | Metrics & More | Article Recommendations | Supporting Information

ABSTRACT: Superionic conductors have great potential as solid-state electrolytes, but the physics of type-II superionic transitions remains elusive. In this study, we employed molecular dynamics simulations, using machine learning force fields, to investigate the type-II superionic phase transition in α-Li_3N. We characterized Li_3N above and below the superionic phase transition by calculating the heat capacity, Li^+ ion self-diffusion coefficient, and Li defect concentrations as functions of temperature. Our findings indicate that both the Li^+ self-diffusion coefficient and Li vacancy concentration follow distinct Arrhenius relationships in the normal and superionic regimes. The activation energies for self-diffusion and Li vacancy formation decrease by a similar proportion across the superionic phase transition. This result suggests that the superionic transition may be driven by a decrease in defect formation energetics rather than changes in Li transport mechanism. This insight may have implications for other type-II superionic materials.

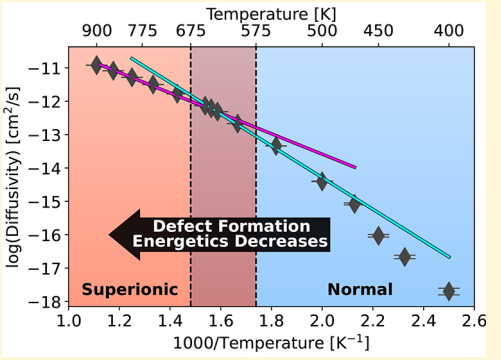

1. INTRODUCTION

Superionic conductors exhibit a thermodynamic phase transition at a temperature T_s, changing from a low ionic conductivity phase to a high ionic conductivity phase. The low temperature and high temperature phases are characterized by their diffusion characteristics and are called the normal and the superionic regimes, respectively.[1−3] The transition from the normal to the superionic regime can be either abrupt (type-I) or continuous (type II). For many superionic conductors, the atomistic mechanisms of ion transport in the superionic regime are not well understood. Furthermore, for type-II superionic transitions, the physical origins of the normal-to-superionic transition are often unclear.[1,2] An improved understanding of ion transport in the superionic regime and the underlying physics of the superionic phase transition could significantly aid the development and optimization of superionic solid electrolytes, with these having potential applications in various devices like fuel cells and all-solid-state batteries.[4−7]

Several mechanisms have been suggested to explain the superionic phase transitions in various superionic solid electrolytes. These include order−disorder transitions,[8−13] competition between local atomic preferences (often described as frustration),[14] and overpopulation of existing lattice sites (sometimes referred to as jamming).[15,16] Moreover, in some materials, the superionic transition is accompanied by significant changes in vibrational spectra. For instance, in $CuCrSe_2$,[11] $AgCrSe_2$,[17] γ-$LiAlO_2$, and Cu_7PSe_6,[18] the superionic transition is linked to a breakdown of specific phonon modes that are dominated by mobile ions.

Vibrational properties have also been studied in the context of materials discovery. When compared to other material descriptors, vibrational properties have been shown to correlate the most with diffusivity[19] and a cheap-to-compute harmonic descriptor, the phonon−band center, was employed in a high-throughput workflow.[20,21] Vibrational descriptors can be further improved by including an anharmonic description of the phonons. Anharmonic descriptors displayed larger correlations with diffusivity when compared to harmonic descriptors,[19] while harmonic and quasi-harmonic descriptions of the phonons failed to provide a signature of the superionic transition in Li_3N.[22]

In this study, we use long-time scale Machine Learning Molecular Dynamics (MLMD) to investigate the behavior of the archetypal superionic conductor Li_3N across the superionic transition. We characterize variations in diffusion, defect, and phonon properties between the normal and superionic regimes and discuss the implications of these changes for ion transport in Li_3N and other type-II superionic conductors.

Li_3N is a structurally and compositionally simple superionic conductor that has been widely studied.[23−38] Li_3N exhibits three crystalline phases: the α-phase (Figure 1), the β-phase,

Received: May 24, 2023
Revised: July 7, 2023
Published: July 19, 2023

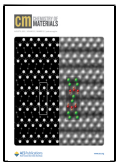

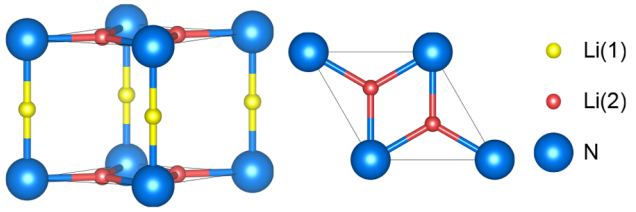

Figure 1. Oblique and top views of the Li_3N structure ($P6/mmm$).

and the γ-phase. The β-phase is thermodynamically stable below 300 K,[22] which is well-below the suggested superionic transition temperature of 588 K < $T_s \leq$ 678 K.[34] The γ-phase is only stable at high pressure.[39] We focus exclusively on α-Li_3N here, which we refer to as Li_3N for simplicity.

Li_3N has a layered structure with alternating layers of Li_2N layers and pure Li, as illustrated in Figure 1. We refer to the Li sites within the pure Li layers as Li(1) and those within the Li_2N layers as Li(2). At 300 K, Li^+ ions in Li_3N undergo three-dimensional diffusion, with a rate of 1.2×10^{-3} S/cm^{-1} in the *ab*-plane and 1×10^{-5} S/cm^{-1} along the *c*-axis.[28] Notable, the rate of 1.2×10^{-3} S/cm^{-1} stood as the highest recorded room-temperature Li^+ ion conductivity for a crystalline phase for many years. Commercial applications of Li_3N, however, have been hindered by a low decomposition potential of 0.45 V versus Li^+/Li.[40]

While Li_3N is often discussed as an archetypal superionic conductor, the existence of a well-defined superionic transition has not been demonstrated. Previous X-ray diffraction data, however, may indicate a superionic transition within the temperature range of 588 K < $T_s \leq$ 678 K.[34] Across this temperature range, the ionic conductivity increases continuously,[29] which would be indicative of a type-II superionic transition. X-ray data from Schulz and Thiemann suggest that the superionic transition would be driven by the increasing amplitude of strongly directional anharmonic vibrations between Li(2) sites and that these anharmonic vibrations would also promote diffusion in the superionic phase.[34]

The diffusion mechanism of Li_3N in the normal regime has been extensively studied using classical Molecular Dynamics (MD),[36,37] *ab initio* Molecular Dynamics (AIMD),[41,42] and nonequilibrium MD.[43] The diffusion mechanism in the superionic regime, however, remains unclear. Studying the dynamics of superionic solid electrolytes both above and below their superionic transition temperature using computer simulation presents a challenge for two reasons. First, conduction mechanisms in the superionic regime are often complex[7,14−16,44−46] and can be sensitive to the exact chemistry of the material under consideration. Therefore, simulation methods that can accurately predict diffusion behavior in the superionic phase should be used, even when there is a lack of experimental data for parametrization. Second, ionic conductivities in the superionic and normal regimes can differ by several orders of magnitude, requiring different simulation time scales to reach long-time diffusive behavior in each case.

AIMD is a powerful tool for studying the dynamics of superionic phases, in part because it does not require parametrization from experimental data. AIMD simulations, however, are computationally costly and are typically limited to simulations of hundreds of atoms over time scales of picoseconds.[47,48] While this can be sufficient to characterize the diffusive regime in a superionic phase, this is often inadequate for studying diffusion at lower temperatures, where ion transport is much slower. Empirical potentials can be used to study long-time scale diffusion behavior in poorly conducting low-temperature systems.[49] These potentials can, however, be challenging to parametrize well and may not equally describe both the normal and superionic regimes.

To address the problem of simulating diffusion in both the normal and superionic regimes, we use Machine Learning Molecular Dynamics (MLMD), training a Gaussian Approximation Potential (GAP)-style[50,51] Machine Learning Force Field (MLFF), using on-the-fly sampling of reference configurations.[52] The resulting MLFF offers near-DFT accuracy without empirical parametrization and has a significantly reduced computational cost compared to direct AIMD simulation. This method allows us to perform simulations of thousands of atoms over nanosecond time scales. Crucially, it also enables us to sample diffusive behavior in both the superionic and normal regimes.

From our MLMD data, we first computed the constant volume heat capacity as a function of temperature. We identify a peak at T_s = 625 K, which we assign as the superionic transition temperature. We observe non-Arrhenius diffusion behavior, characterized by a discontinuous change in the activation energy for the Li^+ self-diffusion coefficient, D^*, at T_s. Analysis of the Li substructure in terms of point defects reveals that some proportion of Li^+ ions move from Li(2) sites, forming Li(2) vacancies and doubly occupied Li(2) or Li(1) sites. Considering Li vacancy concentrations as a function of temperature reveals behavior similar to that for the Li^+ self-diffusion coefficient. Li(2) vacancy concentrations show non-Arrhenius behavior with a discontinuous change in formation activation energy at T_s. The relative change in the Li(2) vacancy formation activation energy across the superionic transition is quantitatively similar to the corresponding change in D^*, which suggests that the superionic transition in Li_3N might be explained by a decrease in the energy required to create defect pairs by displacing Li^+ ions from the Li(2) sites at T_s.

Through an analysis of time-averaged Li^+ densities, we identify two local diffusion pathways between Li(2)−Li(2) and Li(2)−Li(1) site pairs. This results in three-dimensional diffusion at all temperatures, with $D^*_{xy} > D^*_z$.

Finally, we assess the variation in calculated phonon line widths as a function of temperature in the normal and superionic regimes. We find that the computational method we use[53] becomes unreliable when non-negligible diffusion occurs on a simulation time scale and that this method is not suitable for discriminating between the normal and superionic regimes. Nevertheless, calculating the full power spectra using a different method that remains reliable under diffusive conditions reveals that all features in the power spectra significantly broaden with increasing temperature, especially above T_s.

2. METHODS

2.1. First-Principles Calculations. First-principles calculations were carried out using Density Functional Theory (DFT). All DFT calculations were performed within the VASP code,[54] using the PBEsol generalized gradient approximation exchange−correlation functional.[55] Projector augmented-wave pseudopotentials were used to model the ion cores,[56,57] while treating the N 2s and 2p, and the Li 1s and 2s electrons as valence electrons. We used 4 × 4 × 4

https://doi.org/10.1021/acs.chemmater.3c01271
Chem. Mater. 2023, 35, 6133−6140

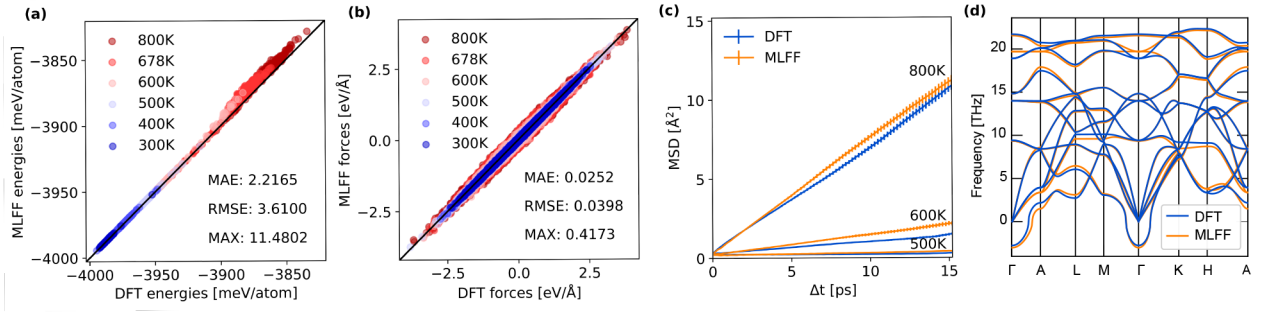

Figure 2. Benchmarking of the machine learning force field with respect to (a) DFT energies (errors in meV/atom), (b) DFT forces (errors in eV/Å), (c) AIMD mean-squared displacements of Li^+ (error bars show estimated confidence intervals of one standard deviation), and (d) DFT harmonic phonons.

Monkhorst–Pack *k*-point meshes to sample the Brillouin zone.[58] *k*-point mesh sizes were reduced for relevant supercell calculations to preserve the net *k*-point density. For geometry optimizations and force calculations, the electronic wave functions were expanded in a plane-wave basis with a kinetic-energy cutoff of 950 eV. The kinetic-energy cutoff was reduced to 400 eV for AIMD and the MLFF training. Geometry optimizations were performed using a quasi-Newton algorithm with a convergence setting of 0.005 eV $Å^{-1}$ for the atomic forces. The resulting optimized structure of Li_3N is shown in Figure 1. The calculated lattice parameters for this DFT-optimized structure compares well with previous computational and experimental data. More detailed information can be found in ref 22.

2.2. Machine Learning Molecular Dynamics. We use MLMD as implemented in VASP.[52,59] In this model, the potential energy U of a structure is approximated by a sum of local atomic energies U_i,

$$U = \sum_{i=1}^{N} U_i \tag{1}$$

where N is the number of atoms in the structure. The local atomic energy of an atom i is assumed to be determined by its local environment, represented as a descriptor that is chosen to be invariant under translations, rotations, and permutations of identical atoms. In this work, we used descriptors based on the smooth overlap of atomic positions (SOAP).[60]

The local environment around an atom i is represented by the neighbor density function ρ_i, which is defined in terms of the positions of atomic neighbors within a cutoff radius R_c,

$$\rho_i(\mathbf{r}) = \sum_j \delta(\mathbf{r} - \mathbf{r}_{ij}) f_{\text{cut}}(|\mathbf{r}_{ij}|) \tag{2}$$

where $\mathbf{r}_{ij} = \mathbf{r}_j - \mathbf{r}_i$ and f_{cut} is a cutoff function, as defined by Behler and Parrinello[61] that smoothly removes information outside R_{cut}. In the descriptors used, the delta function $\delta(\mathbf{r})$ is replaced by a normalized Gaussian function, and the set of these Gaussian functions is used to define rotationally invariant functions, each comprised of a radial distribution function $\rho_i^{(2)}$ and an angular distribution function $\rho_i^{(3)}$. The radial and angular distribution functions are expanded in terms of Bessel functions, which are used as radial basis functions for $\rho_i^{(2)}$ and $\rho_i^{(3)}$. The angular distribution function is also expended in terms of spherical harmonics, which are the angular basis functions. The expansion coefficients of the radial and angular neighbor densities are collected into a vector to form the descriptor of the configuration of atom i as $\mathbf{X}_i$. A Gaussian Approximation Potential (GAP)[62] is used to relate the descriptors to the atomic potential energy U_i. The potential is defined by a set of N_B training configurations $\{ \mathbf{X}_{i_B} \mid i_B = 1, ..., N_B \}$ and fitting parameters w_{i_B}, with similarity between two configurations measured using a polynomial kernel K:

$$U_i = \sum_{i_B=1}^{N_B} w_{i_B} K(\mathbf{X}_i, \mathbf{X}_{i_B}) \tag{3}$$

The coefficients w_{i_B} are optimized using Bayesian linear regression to map reference configurations to their *ab initio* energies per atom and their forces and stress tensors.

2.2.1. Training. We trained a Machine Learning Force Field (MLFF) for Li_3N using an on-the-fly method, as implemented in VASP.[52] This method generates a training data set by performing hybrid AIMD + MLMD simulations, with first-principle *ab initio* steps performed only when local environments that differ significantly from the set of environments already stored as training data are encountered. Newly encountered local environments, and their associated energies, forces, and stresses, are stored in the training data set. This on-the-fly method has proven to be successful at predicting the melting points of Al, Si, Ge, Sn, and MgO,[52] as well as the phase transitions in hybrid perovskites.[59]

In this work, we performed training in a canonical (N, V, T) ensemble using a Nosé–Hoover thermostat. We chose a canonical ensemble over an isobaric–isothermic (N, p, T) ensemble because we found volume effects (Figure S4) to be marginal for the properties we investigated.[22] We note, however, that including volume effects would likely increase defect populations as it would reduce Li–Li repulsion when forming split interstitials. Nevertheless, since the volume expansion is small over the temperature range investigated, we assume that this effect will also be small. MD simulations with a variable cell volume were, therefore, unnecessary. We used a 4 × 4 × 4 supercell for the training, and all MD simulations were run with a time step δt = 2 fs.

For the force-field generation, radial and angular cutoffs were both set to 5 Å. We used Gaussian functions with a width of 0.5 Å to broaden the atomic distributions used for both descriptors. The radial and angular descriptors were expanded by using eight radial basis functions. The MLFF training involved an initial 100 ps heating run from 300 to 1000 K, followed by training for 100 ps at 300 K, 100 ps at 600 K, 500 ps at 678 K, and 200 ps at 900 K. The range of temperatures used in training our MLFF includes temperatures well-below, well-above, and around the experimentally proposed superionic transition temperature. After the complete training routine, the training data set included 659 DFT structures. The final MLFF was constructed using 2553 Li and 595 N local reference configurations.

2.2.2. Validation. To validate our MLFF, we compared per-configuration energies and forces, plus Li^+ mean square displacement (MSD), and harmonic phonons, calculated using our MLFF versus DFT calculations (Figure 2). To generate a new data set of structures distinct from the training data set, we used AIMD simulations performed at 300, 400, 500, 600, 678, and 800 K from our previous work on Li_3N.[22] At each temperature, we performed 10 independent AIMD simulations using different random seeds. Each simulation was run for 8000 steps, giving a total of 160 ps of independent trajectory data at each temperature. To obtain energies and forces, we randomly selected 20 structures per independent trajectory for each temperature, giving a total of 1200 random structures. We then performed single-point calculations on each of these structures using DFT and

https://doi.org/10.1021/acs.chemmater.3c01271
Chem. Mater. 2023, 35, 6133–6140

MLFF and calculated the Root Mean Squared Errors (RMSE), Mean Absolute Errors (MAE), and MAXimum absolute errors (MAX) between the DFT and MLFF data. As expected, the errors in energies are larger at higher temperatures due to the complex local environments observed when diffusion occurs at such temperatures.

We calculated the MSD and their uncertainties over a time scale of 15.4 ps, averaging over each set of 10 independent runs obtained with AIMD and MLMD. We excluded the first 300 steps of each simulation to ensure that only diffusive motion was investigated. The MSD benchmark shows quantitatively similar behavior for both AIMD and MLMD simulations, indicating that diffusion is well described at high temperatures.

To compute the harmonic phonon dispersion, we computed harmonic force constants within a $2 \times 2 \times 2$ supercell using the finite-difference method implemented in PHONOPY.[63] For the DFT-based force calculations, the plane-wave energy cutoff was set to 400 eV, which is the value used for the MLFF training. Good agreement is observed between DFT and MLFF for energies, forces, MSD, and harmonic phonons. The MLFF has near-DFT accuracy, which gives us confidence in the results presented in this study.

2.2.3. Production. For the calculation of all properties excluding anharmonic phonons, we used 1 ns simulation runs in an $8 \times 8 \times 8$ supercell of 2054 atoms. We ran simulations at 200, 250, 300, 350, 400, 430, 450, 470, 500, 550, 600, 630, 640, 650, 700, 750, 800, 850, and 900 K. For anharmonic phonons, we used production runs ranging from 500 ps to 3.5 ns in a $4 \times 4 \times 4$ supercell of 254 atoms, so that the data produced could be compared directly to those from our previous study using AIMD to model the phonon properties of Li_3N.[22] In this part of the study, we ran simulations at 450, 500, 600, 678, and 800 K.

2.3. Heat Capacity. The heat capacity at constant volume, C_V, was estimated numerically via[64]

$$C_V(T) = \left(\frac{\Delta E}{\Delta T}\right)_V \tag{4}$$

$C_V(T)$ was obtained from central differentiation. MLMD simulations were performed at temperatures T_1 and T_2, where $\Delta T = T_2 - T_1$. We then extract the corresponding mean internal energies of the simulations E_1 and E_2, where $\Delta E = E_2 - E_1$. The simulations ran at temperatures ranging from 200 to 900 K with a constant $\Delta T = 50$ K were used to calculate the heat capacity.

2.4. Lithium Transport. To characterize Li^+ transport, we calculate Li^+ mean-squared displacements (MSD) as a function of time interval Δt via

$$\mathrm{MSD}(\Delta t) = \left\langle \frac{1}{N_{\mathrm{Li}}} \sum_{i}^{N} [\mathbf{r}_i(t + \Delta t) - \mathbf{r}_i(t)]^2 \right\rangle \tag{5}$$

where N_{Li} is the number of Li^+ and the angle brackets denote an average over time origins. The self-diffusion coefficient, D^*, is related to the long-time slope of the MSD by the Einstein relation

$$D^* = \lim_{\Delta t \to \infty} \frac{\mathrm{MSD}(\Delta t)}{2d\Delta t} \tag{6}$$

where d is the dimensionality of the system. All diffusion analysis was performed using KINISI, which uses Bayesian linear regression to estimate D^* via Markov-chain Monte Carlo (MCMC) sampling of linear models, $\mathbf{m} = 2dD^*\mathbf{\Delta t} + c$, that are consistent with the observed simulation data.[65] The temperature dependence of D^* was modeled using the exponential form of the Arrhenius expression

$$D^*(T) = A \exp(-E_a/kT) \tag{7}$$

where E_a is the self-diffusion activation energy. "Best fit" Arrhenius relationships were determined using nonlinear Bayesian regression, with the full posterior distribution $p(D^*)$ at each simulation temperature used as inputs. Only converged D^* values obtained for simulations where the diffusive regime was reached within the simulation time scale ($T \geq 400$ K) were used in this part of the analysis.

We also compute time-averaged probability densities of the Li^+ ions, $P(\mathbf{r}_j)$, by projecting the MLMD trajectory onto a uniform 3D grid and calculating the time-average number of atoms at each grid point.[66]

2.5. Site-Projection Analysis. To analyze the mechanistic details of ion transport, we perform a site-projection analysis.[67] This involves projecting the positions of Li^+ ions at each simulation step onto discrete bounded volumes, which correspond to "sites" within the host structure. We define two Li sites using Voronoi decomposition of the simulation volume, with the crystallographic Li(1) and Li(2) positions used as seeds for the Voronoi cells. By projecting instantaneous Li^+ positions onto these Voronoi cells, we can identify and count sites that are vacant or doubly occupied. These sites can formally be described as vacancy- or split-interstitial-type defects. We model the temperature dependence of these defect concentrations using an exponential Arrhenius-like model,

$$[V_{\mathrm{Li}}] = [\mathrm{Li}] \exp(-E_f/2kT) \tag{8}$$

where $[\mathrm{Li}] = [\mathrm{Li}(1)] + [\mathrm{Li}(2)]$ and E_f is an effective vacancy-formation energy. To fit this model, we use the mean observed defect concentrations from our simulations at each temperature as input and fit using nonlinear least squares. For consistency, we restrict ourselves to simulations where the diffusive regime was reached within the simulation time scale ($T \geq 400$ K) in this part of the analysis.

3. RESULTS

3.1. Superionic Phase Transition. To analyze our MLMD simulation trajectories, we compute the constant volume heat capacity, C_V, the Li^+ self-diffusion coefficient, D^*, and the concentration of defects at each simulation temperature.

The calculated constant volume heat capacities (Figure 3) show a heat capacity peak at $T = 625$ K, and we, therefore,

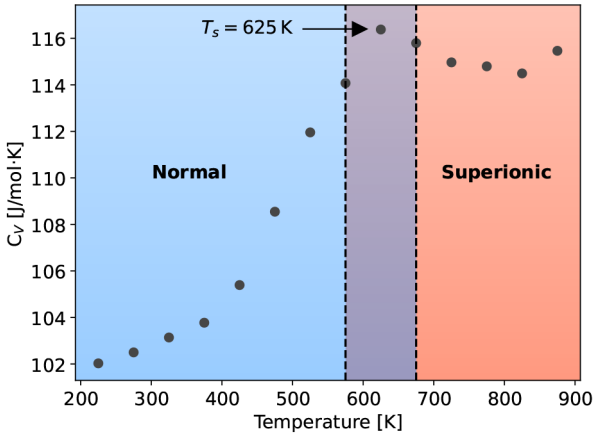

Figure 3. Calculated constant volume heat capacity as a function of temperature. T_s is assigned as the temperature value at the heat capacity peak.

assign the superionic transition temperature, T_s, to this value. We note that our assignment of T_s is limited by our temperature step $\Delta T = 50$ K, and the "real" peak value could be found anywhere in the range 575 K < T_s < 675 K highlighted in Figure 3. Our predicted range for T_s is consistent with the range suggested by Schulz and Thiemann of between 588 and 678 K.[34] A finer $\Delta T = 10$ K was tested to refine our estimation of T_s; however, we observed a discontinuity at $T = 645$ K (Figure S5), which suggests that the energies obtained from the current generation of molecular dynamics trajectories are not converged enough with respect to

https://doi.org/10.1021/acs.chemmater.3c01271
Chem. Mater. 2023, 35, 6133−6140

simulation time and supercell size to use a finer grid than ΔT = 50 K. We also note the slight rise in C_V around 875 K, which may come from premelting phenomena (T_m = 1087 K), or larger errors on energies at higher temperatures (Figure 2(a)).

Our calculated self-diffusion coefficients over the complete range of simulation temperatures exhibit non-Arrhenius behavior (Figure 4(a)); the gradient $d \ln D^*/dT$ is smaller at high temperature, corresponding to a lower activation energy, than at low temperature. By subdividing our self-diffusion coefficient data into low-temperature "normal" (T < 675 K) and high-temperature "superionic" (T > 575 K) subsets, we find two regimes with distinct Arrhenius behaviors. Distinct Arrhenius behaviors in the normal and superionic regimes have been observed in other superionic conductors including fluorites[9] and $AgCrSe_2$.[10] From our D^*_{xyz} data, we assign activation energies of $E_{a,n}$ = 0.4097(8) eV and $E_{a,s}$ = 0.2636(3) eV to the normal and superionic regimes of Li_3N within a 95% confidence interval, respectively. We note that D^*_{xy} and D^*_z follow the same Arrhenius relationships as D^*_{xyz} and hence share the same activation energy barriers in the normal and superionic regimes. Nevertheless, $D^*_{xy} > D^*_z$ at all temperatures, and the ratio D^*_{xy}/D^*_z decreases with temperature, which agrees with the experimentally observed decrease in conductivity anisotropy reported for Li_3N single crystals.[28] The change in self-diffusion activation energy across the superionic transition temperature suggests a corresponding change in how Li^+ ions migrate: either the ease with which individual ions migrate or a change in the fraction of Li^+ ions that participate in diffusion in a given time window.

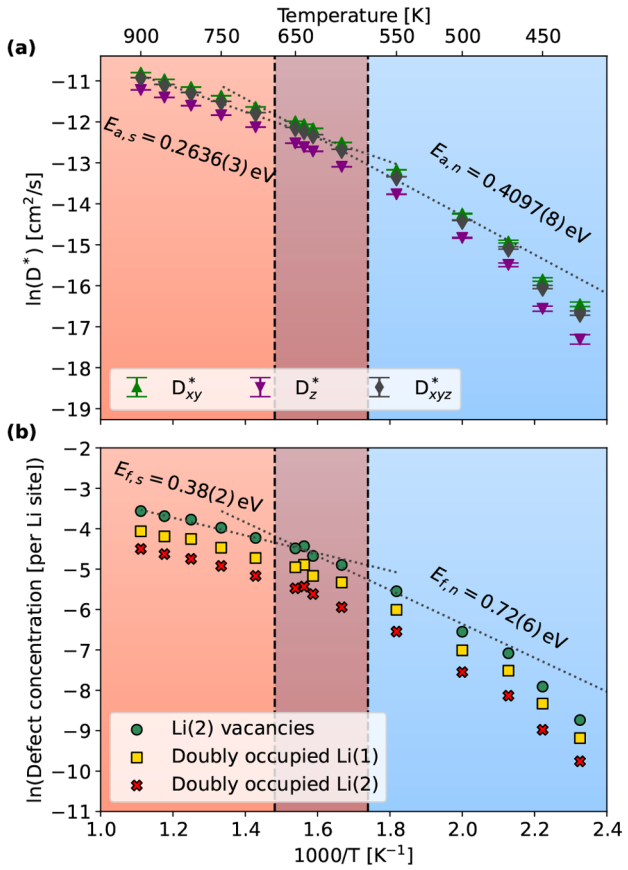

Figure 4. (a) Estimated directionally resolved self-diffusion coefficients, D^*, and (b) defect concentrations as functions of temperature. Self-diffusion coefficient error bars show credibility intervals of 1 standard deviation. The blue and red shaded regions indicate temperatures above or below the superionic transition temperature range 575 K < T_s < 675 K. The dotted lines show fitted Arrhenius relationships to the high-temperature "superionic" and low-temperature "normal" data.

By projecting Li-ion positions onto Li(1) and Li(2) sites, we find that Li(2) sites become increasingly vacant with increasing temperature, while both Li(1) and Li(2) sites exhibit some double occupation (Figure 4(b)). Li(1) sites, on the other hand, are always occupied.

Similar to our analysis of the self-diffusion coefficient D^*, we separate our Li-defect concentration data into normal and superionic subsets, which results in two regimes that exhibit distinct Arrhenius relationships. From our Li(2) vacancy concentration data, we assign defect formation energies of $E_{f,n}$ = 0.72(6) eV and $E_{f,s}$ = 0.38(2) eV to the normal and superionic regimes within a 95% confidence interval, respectively. This change may be attributed to defect−defect interactions that lower the average formation energy at a critical defect concentration reached at T_s. The fraction of Li sites that are vacant reaches a value of 1% at $\approx T_s$. Across the superionic transition, the defect formation energies decrease by a similar factor as for the diffusion activation energies, compared to their low-temperature values. This result suggests that the superionic transition is facilitated by a decrease in the defect formation energy at T_s. Low migration energy barriers, E_m, calculated from nudged elastic band,[68] already suggested that the bottleneck for diffusion came from E_f and not E_m.

The data presented in Figures 3 and 4 demonstrate that Li_3N undergoes a superionic transition, where previous experimental measurements could only suggest such a transition.[34]

3.2. Ion Diffusion Pathways. Examination of time-averaged Li^+ densities shows the presence of diffusion channels between both Li(2)−Li(2) sites and Li(1)−Li(2) sites (Figure 5), which appear unchanged with temperature. In the previous section, using site-projection analysis, we identified that Li(2) sites become vacant, allowing Li^+ to diffuse, while both Li(1) and Li(2) sites become doubly occupied. Figure 5 and temperature-dependent radial distribution functions (Figure S6) show that Li^+ that are displaced from their crystallographic positions are not accommodated as conventional interstitial

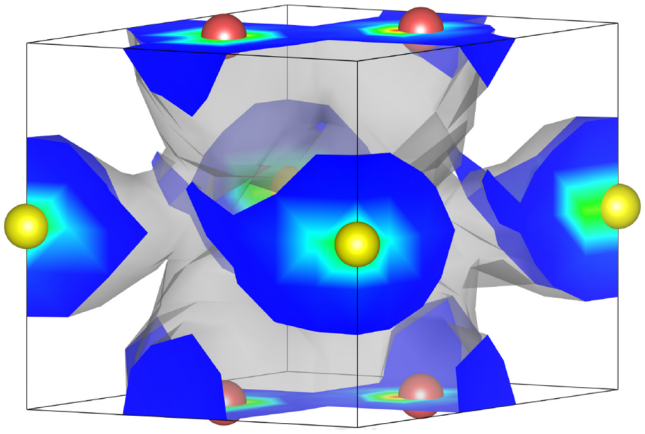

Figure 5. Time-averaged Li^+ density at 650 K, showing diffusion channels between both Li(2)−Li(2) and Li(1)−Li(2) sites.

https://doi.org/10.1021/acs.chemmater.3c01271
Chem. Mater. 2023, 35, 6133−6140

point defects but instead form split interstitial defects through double-occupation of Li(1) or Li(2) sites.

Combining our observations from site-projection analysis and time-averaged particle densities suggest that, by using MLMD, we observe a similar diffusion mechanism to the one described by Mulliner et al. using nonequilibrium MD.[43] They proposed that Li^+ ions were able to leave their Li(2) sites, creating vacancies in the conduction layer, to form Li_2 pairs. Two dimer configurations were suggested: one formed with an ion at another Li(2) site (vertical dimer) and another with an ion located at a Li(1) site (horizontal dimer). Previous studies using AIMD[41,42] and classical MD[36,37] suggested that Li^+ forms similar split interstitials around Li(1) sites. In ref 42, Li(2) split interstitials were also observed. The observations listed here are consistent with the split interstitials that emerge in our trajectories (Figure 4(b)), highlighting MLMD as the method of choice to study ionic conductors.

3.3. Effect of Diffusion on Anharmonic Lattice Dynamics. A computational phonon breakdown of all phonon modes at $T > T_s$ was previously predicted using AIMD and taken as a signature of the superionic phase.[22] The diffusive regime, however, could not be simulated for $T < T_s$ due to the limited simulation time scale, and it was unclear whether the computational phonon breakdown was a consequence of Li^+ ions being mobile on the simulation time scale, or of the superionic transition occurring at T_s. We now have the opportunity to reassess our conclusions using MLFF-based simulations. Within the time scales that are achievable by our MLFF, we are able to simulate the diffusive regime for temperatures as low as 450 K.

To calculate phonon lifetimes at different temperatures from the MLMD trajectories, we used DYNAPHOPY.[53] The methodology for projection onto bulk harmonic phonon eigenvectors and the associated line width calculations is described in Supporting Note I. We find that this approach, used in our previous report for shorter MD time scales,[22] is not suitable when non-negligible diffusion occurs in the simulation. These projections onto bulk phonon modes cannot be used to discriminate between the normal and superionic diffusion regimes. We stress that this result is an effect of the limitations of projecting diffusional dynamics onto a set of bulk phonon eigenvectors; it is not due to a breakdown of lattice dynamics theory under diffusive conditions. This point is discussed further in Supporting Note I and Figure S1.

Since the projection onto the bulk phonon eigenvector fails, we calculate the full power spectra without *a priori* projection and investigate how they vary with temperature (Supporting Note II and Figure S2). It is difficult to perform quantitative analysis on the data, but qualitative insight can be gained. The full shape of the power spectra remains distinguishable at all temperatures; however, all features significantly broaden with increasing temperature, especially above T_s.

4. CONCLUSIONS

We used machine learning force fields to sample diffusive properties of Li_3N above and below the superionic transition. From the calculated values of the heat capacity at a constant volume, we identify the superionic transition temperature of Li_3N to be $T_s \approx 625$ K. The normal and superionic regimes are found to fit two distinct Arrhenius relationships for self-diffusion coefficients and defect concentrations. The activation energies for self-diffusion and Li vacancy formation decrease by a similar factor across the superionic phase transition, which suggests that the superionic transition may be mediated by a decrease in defect formation energetics. We suggest that defect−defect interactions may be responsible for lowering the formation energy at a critical defect concentration reached at T_s.

Analysis of time-averaged Li^+ densities reveals two local diffusion pathways between Li(2)−Li(2) and Li(2)−Li(1) site pairs, giving three-dimensional diffusion at all temperatures, with $D^*_{xy} > D^*_z$. According to our analysis, however, the diffusion pathways remain unchanged with temperature.

Looking beyond Li_3N, a consequence of this work is that the superionic phase transition in type-II superionic materials may be understood as a decrease in defect formation energetics. More effort is needed to understand how defect formation and defect−defect interactions are related across the superionic phase transition so as to identify what material characteristics may facilitate defect formation and drive the superionic transition.

■ ASSOCIATED CONTENT

Supporting Information

The Supporting Information is available free of charge at https://pubs.acs.org/doi/10.1021/acs.chemmater.3c01271.

Anharmonic lattice dynamics methodology, data and discussion; Haven ratio methodology, data and discussion; temperature-dependent volume effects; effect of ΔT step on C_V data; temperature-dependent radial distribution functions; site-analysis methodology and data; and temperature-dependent vacancy probability density (PDF)

■ AUTHOR INFORMATION

Corresponding Authors

Benjamin J. Morgan − *Department of Chemistry, University of Bath, Bath BA2 7AY, United Kingdom;* orcid.org/0000-0002-3056-8233; Email: b.j.morgan@bath.ac.uk

Aron Walsh − *Department of Materials, Imperial College London, London SW7 2AZ, United Kingdom; Department of Physics, Ewha Womans University, Seoul 03760, Korea;* orcid.org/0000-0001-5460-7033; Email: a.walsh@imperial.ac.uk

Authors

Gabriel Krenzer − *Department of Materials, Imperial College London, London SW7 2AZ, United Kingdom;* orcid.org/0000-0003-0074-4424

Johan Klarbring − *Department of Materials, Imperial College London, London SW7 2AZ, United Kingdom; Department of Physics, Chemistry and Biology (IFM), Linköping University, SE-581 83 Linköping, Sweden*

Kasper Tolborg − *Department of Materials, Imperial College London, London SW7 2AZ, United Kingdom; I-X, Imperial College London, London W12 0BZ, United Kingdom;* orcid.org/0000-0002-0278-115X

Hugo Rossignol − *School of Physics, Trinity College, Dublin 2, Ireland; CRANN Institute, Trinity College, Dublin 2, Ireland;* orcid.org/0000-0002-9243-4708

Andrew R. McCluskey − *European Spallation Source ERIC, 2200 København N, Denmark;* orcid.org/0000-0003-3381-5911

Complete contact information is available at: https://pubs.acs.org/10.1021/acs.chemmater.3c01271

https://doi.org/10.1021/acs.chemmater.3c01271
Chem. Mater. 2023, 35, 6133−6140

Author Contributions

Author contributions are listed according to the CRediT system. G.K. contributed to conceptualization, data curation, formal analysis, investigation, validation, visualization, writing of the original draft, and manuscript review and editing. J.K. contributed to conceptualization, formal analysis, and manuscript review and editing. K.T. contributed to conceptualization, formal analysis, and manuscript review and editing. H.R. contributed to methodology and manuscript review and editing. A.R.M. contributed to software and manuscript review and editing. B.J.M. contributed to formal analysis, supervision, and manuscript review and editing. A.W. contributed to conceptualization, funding acquisition, project administration, resources, supervision, and manuscript review and editing.

Notes

The authors declare no competing financial interest.

■ ACKNOWLEDGMENTS

G.K. thanks Abel Carreras for support using DYNAPHOPY and Samuel W. Coles and Chang-Eun Kim for helpful discussions. G.K. and A.W. acknowledge the Faraday Institution for funding a PhD studentship (faraday.ac.uk; EP/S003053/1), grant number FIRG025. J.K. acknowledges support from the Swedish Research Council (VR) program 2021-00486. K.T. acknowledges support from the Eric and Wendy Schmidt AI in Science Postdoctoral Fellowship, a Schmidt Futures program. H.R. acknowledges the Irish Research Council for financial support of a PhD studentship as part of the Irish Research Council Advanced Laureate Award (IRCLA/2019/127). B.J.M. acknowledges support from the Royal Society (Grants UF130329 and URF/R/191006). We are also grateful to the UK Materials and Molecular Modelling Hub for computational resources, which is partially funded by EPSRC (EP/P020194/1).

■ REFERENCES

(1) Boyce, J. B.; Huberman, B. A. Superionic conductors: Transitions, structures, dynamics. *Phys. Rep.* **1979**, *51*, 189−265.
(2) Hull, S. Superionics: Crystal structures and conduction processes. *Rep. Prog. Phys.* **2004**, *67*, 1233.
(3) Cazorla, C.; Errandonea, D. Is the normal to superionic transformation occurring in type-II fast-ion conductors a real thermodynamic phase transition? *arXiv:2008.03627* **2020**, DOI: 10.48550/arXiv.2008.03627.
(4) Goodenough, J. B.; Singh, P. Review−Solid electrolytes in rechargeable electrochemical cells. *J. Electrochem. Soc.* **2015**, *162*, A2387−A2392.
(5) Jay, E.; Rushton, M.; Chroneos, A.; Grimes, R.; Kilner, J. Genetics of superionic conductivity in lithium lanthanum titanates. *Phys. Chem. Chem. Phys.* **2015**, *17*, 178−183.
(6) Famprikis, T.; Canepa, P.; Dawson, J. A.; Islam, M. S.; Masquelier, C. Fundamentals of inorganic solid-state electrolytes for batteries. *Nat. Mater.* **2019**, *18*, 1278−1291.
(7) Morgan, B. J. Understanding fast-ion conduction in solid electrolytes. *Philosophical Transactions of the Royal Society A* **2021**, *379*, 20190451.
(8) Zhang, H.; Wang, X.; Chremos, A.; Douglas, J. F. Superionic UO_2: A model anharmonic crystalline material. *J. Chem. Phys.* **2019**, *150*, 174506.
(9) Eapen, J.; Annamareddy, A. Entropic crossovers in superionic fluorites from specific heat. *Ionics* **2017**, *23*, 1043−1047.
(10) Wang, J.; Ding, J.; Delaire, O.; Arya, G. Atomistic mechanisms underlying non-arrhenius ion transport in superionic conductor $AgCrSe_2$. *ACS Applied Energy Materials* **2021**, *4*, 7157−7167.
(11) Niedziela, J. L.; et al. Selective breakdown of phonon quasiparticles across superionic transition in $CuCrSe_2$. *Nat. Phys.* **2019**, *15*, 73−78.
(12) Hu, Q.; et al. Observation of specific optical phonon modes dominating Li ion diffusion in γ-$LiAlO_2$ ceramic. *Ceram. Int.* **2021**, *47*, 17980−17985.
(13) Bernstein, N.; Johannes, M.; Hoang, K. Origin of the structural phase transition in Li_7La_3 Zr_2 O_{12}. *Physical review letters* **2012**, *109*, 205702.
(14) Wood, B. C.; et al. Paradigms of frustration in superionic solid electrolytes. *Philosophical Transactions of the Royal Society A* **2021**, *379*, 20190467.
(15) He, X.; Zhu, Y.; Mo, Y. Origin of fast ion diffusion in superionic conductors. *Nat. Commun.* **2017**, *8*, 15893.
(16) Annamareddy, A.; Eapen, J. Low dimensional string-like relaxation underpins superionic conduction in fluorites and related structures. *Sci. Rep.* **2017**, *7*, 44149.
(17) Ding, J.; et al. Anharmonic lattice dynamics and superionic transition in $AgCrSe_2$. *Proc. Natl. Acad. Sci. U. S. A.* **2020**, *117*, 3930−3937.
(18) Gupta, M. K.; et al. Strongly anharmonic phonons and their role in superionic diffusion and ultralow thermal conductivity of Cu_7PSe_6. *Adv. Energy Mater.* **2022**, *12*, 2200596.
(19) López, C.; Emperador, A.; Saucedo, E.; Rurali, R.; Cazorla, C. Universal ion-transport descriptors and classes of inorganic solid-state electrolytes. *Materials horizons* **2023**, *10*, 1757−1768.
(20) Muy, S.; et al. Tuning mobility and stability of lithium ion conductors based on lattice dynamics. *Energy Environ. Sci.* **2018**, *11*, 850−859.
(21) Muy, S.; et al. High-throughput screening of solid-state Li-ion conductors using lattice-dynamics descriptors. *iScience* **2019**, *16*, 270−282.
(22) Krenzer, G.; Kim, C.-E.; Tolborg, K.; Morgan, B. J.; Walsh, A. Anharmonic lattice dynamics of superionic lithium nitride. *Journal of Materials Chemistry A* **2022**, *10*, 2295−2304.
(23) Zintl, E.; Brauer, G. Konstitution des lithiumnitrids. *Zeitschrift für Elektrochemie und Angewandte Physikalische Chemie* **1935**, *41*, 102−107.
(24) Masdupuy, E. *Contribution à l'etude des nitrures, des acétylures et des siliciures, mise en évidence de l'ion N3*; Masson et Cie, 1957.
(25) Bishop, S.; Ring, P.; Bray, P. NMR studies of ^{7}Li in polycrystalline lithium nitride. *J. Chem. Phys.* **1966**, *45*, 1525−1531.
(26) Rabenau, A.; Schulz, H. Re-evaluation of the lithium nitride structure. *Journal of the Less Common Metals* **1976**, *50*, 155−159.
(27) Boukamp, B.; Huggins, R. Lithium ion conductivity in lithium nitride. *Phys. Lett. A* **1976**, *58*, 231−233.
(28) Alpen, U. v.; Rabenau, A.; Talat, G. Ionic conductivity in Li_3N single crystals. *Appl. Phys. Lett.* **1977**, *30*, 621−623.
(29) Boukamp, B.; Huggins, R. Fast ionic conductivity in lithium nitride. *Mater. Res. Bull.* **1978**, *13*, 23−32.
(30) Wahl, J.; Holland, U. Local ionic motion in the superionic conductor Li_3N. *Solid State Commun.* **1978**, *27*, 237−241.
(31) Schulz, H.; Schwarz, K. Is there an N^{3-} ion in the crystal structure of the ionic conductor lithium nitride (Li_3N)? *Acta Crystallographica Section A: Crystal Physics, Diffraction, Theoretical and General Crystallography* **1978**, *34*, 999−1005.
(32) Chandrasekhar, H.; Bhattacharya, G.; Migoni, R.; Bilz, H. Infrared and raman spectra and lattice dynamics of the superionic conductor Li_3N. *Phys. Rev. B* **1978**, *17*, 884.
(33) Osborne, D. W.; Flotow, H. E. Lithium nitride (Li_3N): heat capacity from 5 to 350*K*and thermochemical properties to 1086*K*. *J. Chem. Thermodyn.* **1978**, *10*, 675−682.
(34) Schulz, H.; Thiemann, K. Defect structure of the ionic conductor lithium nitride (Li_3N). *Acta Crystallographica Section A: Crystal Physics, Diffraction, Theoretical and General Crystallography* **1979**, *35*, 309−314.
(35) Lapp, T.; Skaarup, S.; Hooper, A. Ionic conductivity of pure and doped Li_3N. *Solid State Ionics* **1983**, *11*, 97−103.

(36) Wolf, M.; Walker, J.; Catlow, C. A molecular dynamics simulation study of the superionic conductor lithium nitride. I. *Journal of Physics C: Solid State Physics* **1984**, *17*, 6623.
(37) Wolf, M.; Catlow, C. A molecular dynamics simulation study of the superionic conductor lithium nitride. II. *Journal of Physics C: Solid State Physics* **1984**, *17*, 6635.
(38) Beister, H. J.; Haag, S.; Kniep, R.; Strössner, K.; Syassen, K. Phase transformations of lithium nitride under pressure. *Angewandte Chemie International Edition in English* **1988**, *27*, 1101−1103.
(39) Gregory, D. H. Lithium nitrides as sustainable energy materials. *Chem. Rec.* **2008**, *8*, 229−239.
(40) Rabenau, A. Lithium nitride and related materials case study of the use of modern solid state research techniques. *Solid State Ionics* **1982**, *6*, 277−293.
(41) Sarnthein, J.; Schwarz, K.; Blöchl, P. Ab initio molecular-dynamics study of diffusion and defects in solid Li_3N. *Phys. Rev. B* **1996**, *53*, 9084.
(42) Kishida, I.; Oba, F.; Koyama, Y.; Kuwabara, A.; Tanaka, I. Variable anisotropy of ionic conduction in lithium nitride: Effect of duplex-charge transfer. *Phys. Rev. B* **2009**, *80*, No. 024116.
(43) Mulliner, A. D.; Battle, P. D.; David, W. I.; Refson, K. Dimer-mediated cation diffusion in the stoichiometric ionic conductor Li_3N. *Phys. Chem. Chem. Phys.* **2016**, *18*, 5605−5613.
(44) Salanne, M.; Marrocchelli, D.; Watson, G. W. Cooperative mechanism for the diffusion of Li^+ ions in $LiMgSO_4F$. *J. Phys. Chem. C* **2012**, *116*, 18618−18625.
(45) Yajima, T.; et al. Correlated li-ion migration in the superionic conductor $Li_{10}GeP_2$ S_{12}. *Journal of Materials Chemistry A* **2021**, *9*, 11278−11284.
(46) Morgan, B. J. Mechanistic origin of superionic lithium diffusion in anion-disordered Li_6PS_5 X argyrodites. *Chem. Mater.* **2021**, *33*, 2004−2018.
(47) Canepa, P. Pushing forward simulation techniques of ion transport in ion conductors for energy materials. *ACS Materials Au* **2023**, *3*, 75−82.
(48) Zuo, Y.; et al. Performance and cost assessment of machine learning interatomic potentials. *J. Phys. Chem. A* **2020**, *124*, 731−745.
(49) Burbano, M.; Carlier, D.; Boucher, F.; Morgan, B. J.; Salanne, M. Sparse cyclic excitations explain the low ionic conductivity of stoichiometric Li_7La_3 Zr_2 O_{12}. *Phys. Rev. Lett.* **2016**, *116*, 135901.
(50) Szlachta, W. J.; Bartók, A. P.; Csányi, G. Accuracy and transferability of gaussian approximation potential models for tungsten. *Phys. Rev. B* **2014**, *90*, 104108.
(51) Dragoni, D.; Daff, T. D.; Csányi, G.; Marzari, N. Achieving DFT accuracy with a machine-learning interatomic potential: Thermomechanics and defects in bcc ferromagnetic iron. *Physical Review Materials* **2018**, *2*, No. 013808.
(52) Jinnouchi, R.; Karsai, F.; Kresse, G. On-the-fly machine learning force field generation: Application to melting points. *Phys. Rev. B* **2019**, *100*, No. 014105.
(53) Carreras, A.; Togo, A.; Tanaka, I. Dynaphopy: A code for extracting phonon quasiparticles from molecular dynamics simulations. *Comput. Phys. Commun.* **2017**, *221*, 221−234.
(54) Kresse, G.; Furthmüller, J. Efficient iterative schemes for ab initio total-energy calculations using a plane-wave basis set. *Phys. Rev. B* **1996**, *54*, 11169.
(55) Perdew, J. P.; et al. Restoring the density-gradient expansion for exchange in solids and surfaces. *Phys. Rev. Lett.* **2008**, *100*, 136406.
(56) Blöchl, P. E. Projector augmented-wave method. *Phys. Rev. B* **1994**, *50*, 17953.
(57) Kresse, G.; Joubert, D. From ultrasoft pseudopotentials to the projector augmented-wave method. *Phys. Rev. B* **1999**, *59*, 1758.
(58) Monkhorst, H. J.; Pack, J. D. Special points for Brillouin-zone integrations. *Phys. Rev. B* **1976**, *13*, 5188.
(59) Jinnouchi, R.; Lahnsteiner, J.; Karsai, F.; Kresse, G.; Bokdam, M. Phase transitions of hybrid perovskites simulated by machine-learning force fields trained on the fly with Bayesian inference. *Physical review letters* **2019**, *122*, 225701.
(60) Bartók, A. P.; Kondor, R.; Csányi, G. On representing chemical environments. *Phys. Rev. B* **2013**, *87*, 184115.
(61) Behler, J.; Parrinello, M. Generalized neural-network representation of high-dimensional potential-energy surfaces. *Physical review letters* **2007**, *98*, 146401.
(62) Bartók, A. P.; Payne, M. C.; Kondor, R.; Csányi, G. Gaussian approximation potentials: The accuracy of quantum mechanics, without the electrons. *Physical review letters* **2010**, *104*, 136403.
(63) Togo, A.; Tanaka, I. First principles phonon calculations in materials science. *Scripta Materialia* **2015**, *108*, 1−5.
(64) Allen, M. P.; Tildesley, D. J. *Computer simulation of liquids*; Oxford University Press, 2017.
(65) McCluskey, A. R.; Coles, S. W.; Morgan, B. J. Accurate estimation of diffusion coefficients and their uncertainties from computer simulation. *arXiv:2305.18244* **2023**, DOI: 10.48550/arXiv.2305.18244.
(66) Zhu, Z.; Chu, I.-H.; Deng, Z.; Ong, S. P. Role of Na^+ interstitials and dopants in enhancing the Na^+ conductivity of the cubic Na_3PS_4 superionic conductor. *Chem. Mater.* **2015**, *27*, 8318−8325.
(67) Morgan, B. J. *site-analysis*; 2020; https://site-analysis.readthedocs.io, last visited 2023-06-23.
(68) Li, W.; et al. Li^+ ion conductivity and diffusion mechanism in α-Li_3 N and β-Li_3 N. *Energy Environ. Sci.* **2010**, *3*, 1524−1530.

https://doi.org/10.1021/acs.chemmater.3c01271
Chem. Mater. 2023, 35, 6133−6140